2018 IEEE Conference on Decision and Control (CDC)
Miami Beach, FL, USA, Dec. 17-19, 2018

POD-based recursive temperature estimation for MR-guided RF hyperthermia cancer treatment: A pilot study

R.W.M. Hendrikx[1], S. Curto[2], Bram de Jager[1], E. Maljaars[1], G.C. van Rhoon[2], M.M Paulides[2], W.P.M.H. Heemels[1]

Abstract— **In this paper, proper-orthogonal-decomposition (POD) reduced models of the body's heat response to radio-frequency hyperthermia cancer treatment are used for recursive temperature estimation. First, efficient low-dimensional models are obtained by projecting high-resolution finite-difference discretized models on low-dimensional subspaces spanned by empirical simulation modes. These models are then used in a Kalman filter to obtain recursive 3D temperature estimates from noise-susceptible magnetic resonance thermometry (MRT). The strategy is tested on an experimental setup containing an anthropomorphic phantom. It is found that recursive estimation reduces the mean absolute temperature error for the phantom experiment by 38% when compared to MRT and may be a valuable addition to MRT, most notably in the case where high quality thermometry is temporally interleaved with thermometry of degraded quality.**

I. INTRODUCTION

Hyperthermia is an additive cancer treatment therapy that enhances the effects of radiotherapy and chemotherapy by locally applying heat to the tumor region. The resulting temperature elevation has toxic effects on tumor tissue due to a multitude of mechanisms, without harming healthy surrounding tissue [1]. Clinical studies have shown that complementing radiotherapy with hyperthermia results in higher response and survival rates [1], [2]. Furthermore, hyperthermia does not increase radiation toxicity and is considered a safe treatment without significant side-effects. An overview of hyperthermia methods and their development can be found in [3], [4]. In this paper, we focus on deep Radio Frequency (RF) hyperthermia treatments in the pelvic region in which a temperature elevation of 3-7 °C has to be maintained for 90 minutes. RF hyperthermia is applied through a phased-array antenna applicator that uses constructive interference to generate the heat focus inside the patient. Individual phases and amplitudes of twelve fixed-frequency antenna-pairs can be controlled to deliver energy with a focus in the tumor region.

Magnetic resonance thermometry (MRT) has made it possible to acquire non-invasive temperature measurements inside the patient, with good spatial resolution, using a standard MRI scanner. This has enabled the use of feedback control (e.g., [5], [6]) to optimize the temperature distribution and to prevent the occurence of hotspots in healthy tissue. Direct feedback control of the temperature distribution requires accurate and frequent MR thermometry acquisition. However, a major problem of MRT is the susceptibility to motion artifacts, caused by organ and internal gas movement in the patient and forced water circulation through a waterbolus surrounding the patient. This forced circulation of water is needed as a cooling mechanism for the patient's skin. It was shown in a study by Gellerman et al. [7] that MRT using the proton resonance frequency shift (PRFS) technique is feasible for deep RF hyperthermia using both a cylindrical and an anthropomorphic phantom. The authors [7] validated the BSD-2000 3D/MR (Pyrexar, Salt Lake City, UT, USA) applicator using advanced measurement processing in which the water inside the bolus was not circulated and the water temperature was measured to correct the MRT temperatures using a polynomial fitting procedure. The authors report mean absolute temperature errors (MAE) with respect to validation probes that range from 0.52 °C with bolus temperature correction to 0.84 °C without correction. However, in real patient studies such as [8] this accuracy decreases to 1.5 °C due to both intra-scan and inter-scan motion. This motion is problematic due to the spatial mismatch of the phase difference relative to the reference image with the PRFS technique (see, e.g., [9]). MRT processing to prevent noise and artefacts is an active field of research where most approaches focus on motion compensation (e.g., [10]) and drift correction (e.g., [11]) algorithms. A different approach is to combine heating models of the human body with measured temperatures. Model-based filtering of measurements in hyperthermia has been proposed for invasive measurements in [12] and MRT data in [13]. However, these studies focused on parameter estimation and did not include experimental validation. For High Intensity Focussed Ultrasound (HIFU) hyperthermia, an extended Kalman filter was proposed by Roujol et al. in [14] and was shown to improve temperature estimates in an *in vivo* experiment. For RF hyperthermia, a recent study by Zhang et al. [15] proposed the use of recursive estimation for MRT enhancement. The authors used a pixel-by-pixel Kalman filter approach to estimate the heat-induced phase change and incorporated this estimate into a hybrid PRFS method [16]. Their paper focuses on improving the parameter settings for the hybrid PRFS method and achieves a reduction

This research has been made possible by the Dutch Cancer Society and the Netherlands Organisation for Scientific Research (NWO) as part of their joint Partnership Programme "Technology for Oncology". This project is partially financed by the PPP Allowance made available by Top Sector Life Sciences & Health. This research is supported by Pyrexar Medical.

[1]Bob Hendrikx, Bram de Jager, Bert Maljaars and Maurice Heemels are with the Control System Technology Group, Department of Mechanical Engineering, Eindhoven University of Technology, Eindhoven, 5600 MB, The Netherlands

[2]Sergio Curto, Gerard van Rhoon and Maarten Paulides are with the Hyperthermia Unit, Department of Radiation Oncology, Erasmus MC Cancer institute, 3008 AE Rotterdam, The Netherlands

in RMS error for a square gel phantom in which a microwave heating probe is inserted.

Although the studies mentioned have focused on model-based filtering, the problem of dealing with large and complex patient models has not yet been adressed in literature. In hyperthermia treatment planning, patient-specific models are already clinically used to determine the power and temperature distribution in response to the electro-magnetic field (see, e.g., [4]). These models are obtained by Computed Tomography (CT) segmentation of the patient and are used prior to treatment to calculate the optimal antenna settings for tumor focus. The availability of these models, indeed, suggests a strategy of combining simulation and MRT during treatment to obtain reliable temperature estimates. However, spatial discretization of temperature models for patient geometries in the pelvic region generally results in very large state space systems, which are often too complex for on-line usage. Hence, enhancing MR thermometry (and ultimately controlling the temperature distribution) requires adequate reduced-order models that enable fast computation times during treatments. Hereto, we propose the use of the simulation-based proper orthogonal decomposition (POD) model reduction technique. While POD for model reduction has attracted much attention in various fields (see, e.g., [17]) including modal identification for hyperthermia (Niu et al. in [18]), the simulation-based application to hyperthermia proposed in this paper is new. The precomputation of patient-specific heating modes enables the use of accurate and efficient models that capture the complexity due to patient geometry well, without compromising spatial resolution.

This paper proposes the application of these models in a recursive estimation strategy to enhance MR thermometry. A strategy is presented in which these reduced models are combined with MR thermometry to make a new *best estimate* of the temperature whenever MRT data is available. This has the potential to reduce the effects of noise and motion artefacts from the MRT and lead to more accurate temperatures. Furthermore, it can allow to reduce the number of times the active patient cooling has to be stopped while acquiring new readings, by mitigating the disturbances caused by water motion; and to rely on simulation data in between consecutive MRT updates. Note that validation of the hyperthermia setup using more advanced PRFS techniques has been discussed in [7] and is not within the scope of this work. The aim of the current paper is to motivate the use of POD-reduced models on complex patient geometries for recursive 3D temperature estimation and to provide a first experimental study.

This paper is structured as follows. First, in section II, the electromagnetic and bioheat models used in RF hyperthermia are introduced. Second, the POD reduction method is explained that reduces the bioheat model by considering a small set of temperature basis vectors (section III). Based on this POD-reduced model, the Kalman filtering strategy is introduced in section IV. In section V, the strategy is tested on a non homogeneous anthropomorphic phantom containing plastic bone structure and thermistor temperature probes in the central transversal plane. Finally, the results of the strategy are discussed in section VI to conclude the paper.

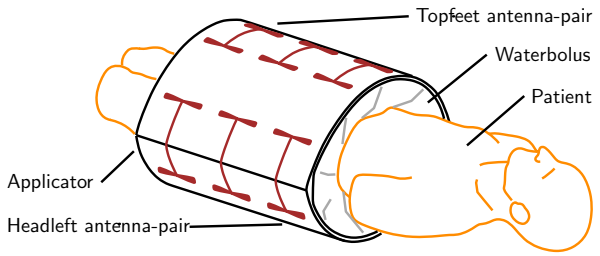

Fig. 1. Schematic depiction of the applicator-patient model with 12 antenna-pairs in three rings.

II. Applicator-patient model

The physical model of the temperature response in hyperthermia is separated into two distinct parts:

(i) The electromagnetic (EM) model, relating applicator phase and power inputs to the power distribution inside the human body.

(ii) The bioheat model, relating power distribution to temperature distribution inside the human body.

The combination of these models will be referred to as *applicator-patient model*.

A. Electromagnetic model

A schematic picture of the applicator-patient setup is shown in Fig. 1. The BSD-2000 3D/MR (Pyrexar, Salt Lake City, UT, USA) applicator consists of three rings, containing four dipole antenna-pairs each. The patient is placed inside the applicator and the waterbolus is filled. The waterbolus serves three purposes; transmitting EM waves efficiently to the body, EM matching of the antennas, and cooling the skin by forced water circulation. The antennas are excited by a 100 MHz wave generator capable of setting individual power and phase on each of the 12 dipole antenna-pairs. The resulting electric fields of the antenna-pairs are calculated by solving Maxwell's equations using a computer simulation. Although these simulations are time-consuming and patient-specific, they can be performed offline before treatment. By the linearity assumption of Maxwell's equations, the total electric field is obtained by superimposing the simulated individual fields, scaled by the applicator inputs, leading to

$$\vec{E}(\vec{r},p)=\sum_{j=1}^{n_p} p_j \vec{E}_j(\vec{r}), \tag{1}$$

where $\vec{r}\in\Omega$ is a point in the patient domain, $\vec{E}:\Omega\to\mathbb{C}^3$ and $\vec{E}_j:\Omega\to\mathbb{C}^3$ are the total electric field and individual anntenna fields, respectively, in complex phasor notation, $p_j\in\mathbb{C}$ are the complex inputs containing phase ($\angle p_j$) and power ($|p_j|^2$) and $n_p=12$ denotes the total number of antennas. The Specific Absorption Rate (SAR) in W/kg is used to quantify the power distribution induced by the electric field as

$$\mathrm{SAR}(\vec{r},p)=\frac{\sigma(\vec{r})}{2\rho(\vec{r})}|\vec{E}(\vec{r},p)|^2, \tag{2}$$

where $\sigma(\vec{r})$ and $\rho(\vec{r})$ denote tissue-dependent (electrical) conductivity and mass-density, respectively. The modeling of EM-induced SAR has been clinically validated in various setups [19], [20]. Furthermore, uncertainty in dielectric tissue properties has been addressed in literature (e.g., [21]). In this paper the SAR distribution resulting from a certain applicator setting is assumed to be a known quantity.

B. Bioheat model

The temperature elevation in response to the SAR distribution is described by a bioheat model. The common Pennes Bio-Heat Equation (PBHE) [22] is used, which takes the general form:

$$\rho c \frac{\partial T}{\partial t} = \nabla \cdot (k \nabla T) + \rho Q_m + \rho \mathrm{SAR} - \rho_b c_b \rho \phi (T - T_b), \quad (3)$$

where k denotes the thermal conductivity, c denotes the specific heat capacity, ϕ denotes the volumetric blood perfusion rate per unit mass tissue, Q_m denotes the metabolic heat generation, SAR denotes the specific absorption rate and the subscript b denotes blood properties. In general, all parameters can vary with tissue region, although dependence on $\vec{r}$ is omitted for brevity. Applying a finite difference spatial discretization to the PBHE leads to the nodal state space representation:

$$\frac{d\xi(t)}{dt} = F\xi(t) + Gq(t) + h(t), \quad (4)$$

where $\xi \in \mathbb{R}^n$ denotes the nodal temperature values, $q(t)$ denotes nodal SAR input, $F, G \in \mathbb{R}^{n \times n}$ are constant matrices and $h(t)$ contains possible non-homogeneous effects due to boundary conditions and blood perfusion.

III. POD model reduction based on snapshots

Heat models resulting from finite-difference discretization on the treatment domain are in the order of $n = 10^5$ states, which is often intractable for on-line use. The POD technique based on simulation snapshots [17] is used to obtain a reduced-order model. This method exploits the fact that the space of physically likely solutions of a system are often described well by a small set of basis functions. The snapshot-based POD method has some properties that make it suitable for a hyperthermia context. Firstly, it leads to accurate representations with only few states. Secondly, it inherently approximates the whole state space and does not require the definition of model outputs for regions of interest; and finally, since it is simulation-based, it provides control over which inputs are captured well by the reduced model. For RF hyperthermia, this input (or set of inputs) can be obtained before treatment by optimizing for tumor focus. Consider a snapshot matrix X, containing (possibly multiple) simulated state trajectories (i.e., solutions) of the system (4) at discrete time instants for inputs of interest given by

$$X = \begin{bmatrix} \xi(t_1) & \xi(t_2) & \cdots & \xi(t_\ell) \end{bmatrix} \in \mathbb{R}^{n \times \ell}. \quad (5)$$

POD aims to reconstruct this trajectory by linear combinations of a set of m basis vectors. A matrix $\hat{X}_m$ of rank $m \leq \ell$, constructed from a set of m orthonormal basis vectors, is a $2-$norm optimal approximation if it minimizes the error:

$$\|X - \hat{X}_m\|_2. \quad (6)$$

This matrix is obtained by making a singular value decomposition (SVD) of X given by

$$X = U \Sigma V^H, \quad (7)$$

and then applying truncation, leading to

$$\hat{X}_m = \sum_{i=1}^{m} \sigma_i u_i v_i^H = U_m \Sigma_m V_m^H, \quad (8)$$

where the vectors $u_1, \cdots, u_m$ form an orthonormal basis for the approximation space and are contained in the matrix U_m. The nodal state vector ξ is now approximated by

$$\xi(t) \approx U_m x(t) \quad (9)$$

with x the reduced state. This reduced state is interpreted as the coefficients of the vectors spanning the approximated solution space.

The reduced system is obtained by applying Galerkin projection of the original model (4) on the orthonormal basis U_m, leading to the reduced dynamics

$$\Sigma_{\text{red}} \triangleq \begin{cases} \dfrac{dx(t)}{dt} = \underbrace{U_m^T F U_m}_{\tilde{A}} x(t) + \underbrace{U_m^T G}_{\tilde{B}} q(t) + \underbrace{U_m^T h(t)}_{\tilde{h}(t)} \\ \xi(t) \approx U_m x(t). \end{cases} \quad (10)$$

IV. Recursive estimation

It is assumed that a POD-reduced model describes the true thermal dynamics well. The linear model (10) is time-discretized between MRT measurement updates, which are available every $t_k, k \in \mathbb{N}$, leading to the system

$$\Sigma_{\text{true}} \triangleq \begin{cases} x_{k+1} &= Ax_k + Bq_k + h_k + w_k \\ \xi_k &= U_m x_k \\ y_k &= CU_m x_k + v_k, \end{cases} \quad (11)$$

where $x_k \triangleq x(t_k) \in \mathbb{R}^m$ is the reduced state vector containing the coefficents for the columns of U_m, $q_k \in \mathbb{R}^n$ is the nodal SAR input vector, $\xi_k \in \mathbb{R}^n$ is the discretized temperature field and $y_k \in \mathbb{R}^{n_y}$ are the *measured outputs* obtained from the MRT data. These nodal values are an interpolation of ξ_k contained in the mapping C. The system matrices (A, B, h_k) are obtained from Σ_{red} in (10) by exact discretization in the update interval (e.g., $A = \int_{t_k}^{t_{k+1}} e^{\tilde{A}\tau} d\tau$). The process and measurement disturbances are accounted for by the vectors $w_k \in \mathbb{R}^m$ and $v_k \in \mathbb{R}^{n_y}$, respectively.

A. Uncertainty estimates

We assume that the disturbances w_k, v_k can be described by zero-mean Gaussian white noise to facilitate the use of a classical Kalman filter. Process noise $w \sim \mathcal{N}(0, W)$ is used to model input and parameter uncertainty. Measurement noise is approximated by $v_k \sim \mathcal{N}(0, V_k)$. Both W and V_k are assumed to be diagonal (i.e., no spatial correlation

between MRT measurement point uncertainty and between modal POD uncertainty) and V_k is time-dependent to capture measurement noise for the current MRT acquisition. In practice, the assumption of Gaussian noise for w is unlikely to hold and W should be interpreted as a model mismatch approximation. It is not trivial to determine this model mismatch before the experiment, especially since W_{ii} is associated with POD mode i. If no region-specific knowledge is available about model uncertainty, a heuristic approximation $W = \sigma_w I$ may be used where σ_w is treated as a model uncertainty weighting. Assuming spatially uncorrelated measurement noise, the measurement covariance V_k can be approximated by the spatial variance around each MRT pixel within the 2D slice given by

$$\sigma_{vi}^2 = \frac{1}{9} \sum_{j \in D(i)} (y_j - \bar{y}_i)^2, \tag{12}$$

where $D(i)$ contains the nodes in a 3-by-3 neighbourhood around the y_i node and $\bar{y}_i$ is the mean temperature in that neighbourhood. The result is a high uncertainty weighting in noisy areas such as movement artefacts, and tissues that are not measurable by the PRFS technique due to low water content. A downside of this method is that regions containing large temperature gradients will have higher covariance estimates as well. In practice, gradients are expected to be small enough to allow this approach.

B. Recursive update scheme

To estimate the state of the reduced-order system Σ_{true}, the classical Kalman observer model is used of the form

$$\Sigma_{\text{est}} \triangleq \begin{cases} \hat{x}_{k+1} & = A_k \hat{x}_k + B_k q_k + h_k + K_k(y_k - \hat{y}_k) \\ \hat{\xi}_k & = U_m \hat{x}_k \\ \hat{y}_k & = C U_m \hat{x}_k, \end{cases} \tag{13}$$

with innovation gain K_k and estimated quantities denoted by the hat superscript. The estimation error is defined for the reduced state as

$$e_k \triangleq \hat{x}_k - x_k \tag{14}$$

with covariance

$$P_k \triangleq \mathbb{E}(e_k - \mathbb{E}e_k)(e_k - \mathbb{E}e_k)^T. \tag{15}$$

The error and covariance of the nodal temperatures can be reconstructed using the projection matrix U_m. For a given initial state estimate $\hat{x}_0 = \mathbb{E}x_0$ and initial error covariance P_0, the optimal estimation $\hat{x}_k$, minimizing $\mathbb{E}e_k^T e_k$, which is equivalent to $\mathbb{E}(\hat{\xi}_k - \xi_k)^T(\hat{\xi}_k - \xi_k)$, is given recursively by the discrete-time Kalman update equations (see, e.g., [23]). At every time instance, the *a priori* estimate of the state and error covariance are first calculated by propagation through the following dynamics:

Model update equations (prediction)

- $P_{k+1}^- = A_k P_k A_k^T + W_k$
- $\hat{x}_k^- = A_k \hat{x}_k + B_k u_k$

The model estimates (denoted with a $-$) are then updated with the available MRT data by the measurement update equations:

Measurement update equations (correction)

- $K_k = P_k^- [CU_m]^T ([CU_m] P_k^- [CU_m]^T + V_k)^{-1}$
- $\hat{x}_k = \hat{x}_k^- + K_k(y_k - CU_m \hat{x}_k^-)$
- $P_k = (I - K_k CU_m) P_k^-$

These update equations compute the optimal innovation gain K_k, leading to the current best estimate of the temperature $\hat{\xi}_k = U_m \hat{x}_k$.

V. Experimental Setup

The reduced-model estimation strategy (POD-Kalman filter) proposed in the previous section is tested using an anthropomorphic phantom placed inside an MR-guided deep hyperthermia setup (*BSD-2000 3D/MR, Pyrexar, Salt Lake City, UT, USA*). Figure 3a shows the phantom, consisting of a plastic shell containing dielectric material that resembles human tissue and plastic bone material resembling a human spine and pelvis. The effect of blood perfusion is not present in the phantom, implying that only thermal conductivity, heat capacity and boundary heat flow are responsible for the thermal response. The setup inside the MRI bore is shown schematically in Fig. 3b. Only the central MRT slice is used. The MRT image (in-plane resolution is 128x128 measurement points) is interpolated to the center plane of the simulation grid.

A. Applicator settings

Two different applicator settings are used, focusing at $(x, y, z) = (3, 0, 0)$ cm and $(-3, 0, 0)$ cm, respectively, in a homogeneous target with a total power of 600 W (right focus and left focus in the central transversal plane). During heating, water from the waterbolus is not circulated, to prevent artefacts in this phase of the study. After applying focus setting 1 to the applicator, six automated scans of 93 seconds each are made. After this period, one scan is obtained with no heating applied. Then another six scans are obtained with focus setting 2 applied. Finally, the applicator is turned off and some extra scans are made, both with the water circulation turned off and while water is circulating, generating measurement disturbance. The experiment timeline is summarized in Fig. 2.

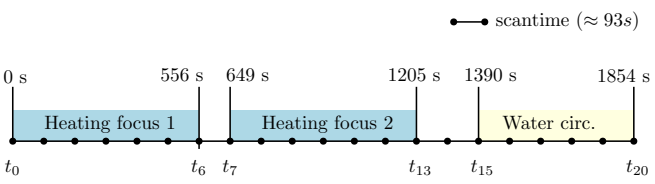

Fig. 2. Scan intervals and applied heating settings during the experiment.

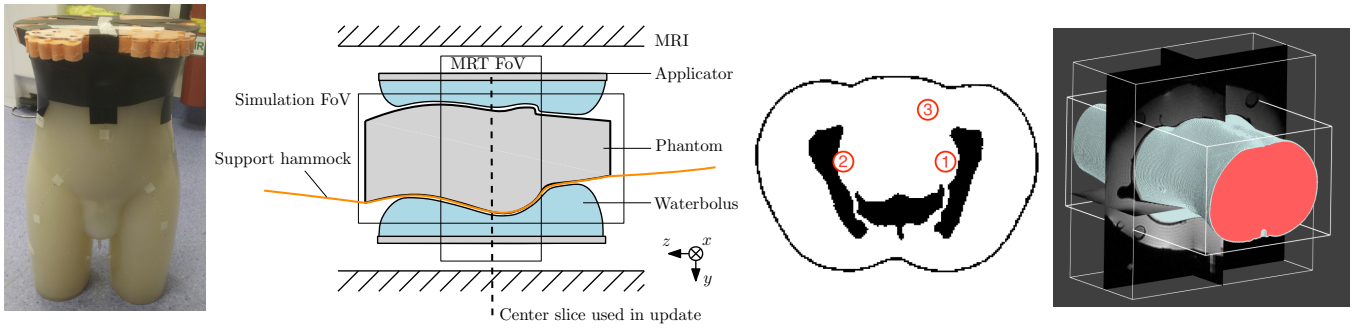

(a) (b) (c) (d)

Fig. 3. (a) The anthropomorphic phantom. (b) A schematic overview of the phantom and applicator inside the MRI bore with the center slice indicated. (c) The location of the thermistor temperature probes in the center slice shown in a CT segmentation. (d) The alignment of the phantom model with respect to the applicator using MRI images imported into the Sim4Life software environment.

B. Temperature monitoring

A total of three thermistor probes are used to measure the temperature with an accuracy of $\sigma = 0.1°C$. The probes were placed in the center transversal slice of the phantom inside catheter tracks, as shown in Fig. 3c by the numbers $1-3$, using a CT imaging scan as a guidance tool. Note that these probes are only used for comparison purposes and are not used in the filter update.

C. EM simulation

The heat source field (SAR) for the thermal simulations is calculated using EM simulations on a CT-segmented 3D model of the phantom. Using MRI images made before the experiment, the positioning of the phantom with respect to the applicator is matched with the experimental setup (see Fig. 3d). The dielectric properties used in the EM simulation are shown in Table I.

TABLE I

DIELECTRIC PROPERTIES FOR THE EM SIMULATION.

Material	ε_r [-]	σ [S/m]
Shell (plastic)	2.8	0
Applicator (plastic)	2.8	0
Bones (plastic)	2.8	0
Water	80.955	0.00263
Soft tissue	78	0.45

D. Temperature simulation and POD reduction

For the thermal simulation, an 8 mm spatially discretized model is created in MATLAB, containing $n = 56,173$ dynamic states and using the thermal properties in Table II. In the simulation, the temperature is defined relative to the baseline temperature (i.e., the deviation from initial phantom temperature which equals the room temperature). Boundary conditions are modeled by convective heat transfer to room temperature ($T_{\text{BC}} = 0$ °C) with $h_{\text{BC}} = 20$ W/m^2/K for air contact and by a Dirichlet condition ($T_{\text{BC}} = 0$ °C) for water contact. A POD basis is generated by simulating the experiment. To provide more degrees of freedom to the POD basis, two extra simulated responses were added to the snapshot matrix. The first additional simulation contains the two focal settings shifted upwards by 3 cm (in the -y direction in Fig. 3b). The second simulation increased thermal conductivity of the soft tissue gel to $k = 5$ to achieve a significant spread to the edges of the phantom. Note that these added simulations do not change the reduced model response directly. They were added to provide more degrees of freedom to the POD basis. Projection on the POD basis of dimension $m = 18$ yields the reduced model Σ_{red} in (10) used in the filter update.

TABLE II

THERMAL PROPERTIES FOR THE THERMAL STATE SPACE MODEL.

Material	c [J/kg/K]	k [W/m/K]	ρ [kg/m^3]
Shell (plastic)	1500	0.2	1000
Soft tissue	3630	0.64	1000
Bones (plastic)	1500	0.2	1600

E. MRT acquisition

The thermometry acquired from the 1.5 Tesla MRI system is processed using the PRFS technique, where the temperature change is calculated from the unprocessed phase images using

$$\Delta T = \frac{\varphi(T) - \varphi(T_0)}{\gamma \alpha B_0 T_E} - \Delta T_{\text{sil}} \tag{16}$$

with $\varphi(T)$ denoting the phase angle of a pixel, T_0 the reference image pixel, γ the gyromagnetic ratio, α the PRFS constant, B_0 the static field strength and T_E the echotime. The pixel-wise average temperature change in silicone tubes in the four corners of the applicator, ΔT_{sil}, is subtracted from the slices to compensate for drifts in the B_0 static magnetic field. The values that are used for the parameters are shown in Table III.

TABLE III

THERMOMETRY CONSTANTS

γ [rad/s/T]	α [C^{-1}]	B_0 [T]	T_E [ms]
$267.5 \cdot 10^6$	$-0.0085 \cdot 10^{-6}$	1.5	19.1

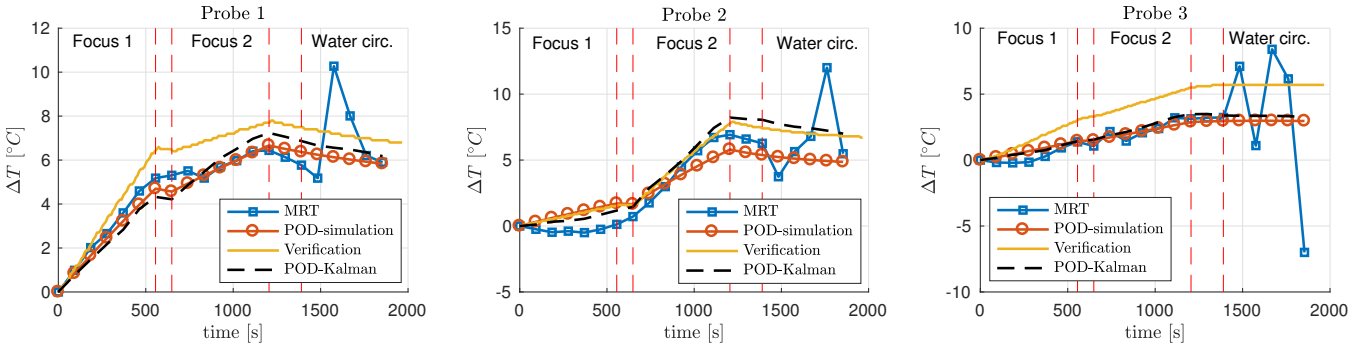

Fig. 4. Temperature response versus time in the probe locations for the POD-reduced forward simulated model, the MR thermometry, the verification probes and the POD-Kalman filter with $\sigma_w = 2$. The dashed vertical line indicates the time points where heating settings were applied and where water circulation was started.

F. Recursive estimation

The observer model (13) is updated using the model and measurement update equations introduced in Section IV. The spatial SAR distribution obtained from the EM simulation is applied in the model update. The measurement covariance is obtained by spatial variance estimation (12). The impact of model uncertainty σ_w^2 is investigated by estimating the full temperature trajectories for three different values of σ_w^2 and calculating the mean absolute temperature error (MAE) with respect to the verification probe values.

G. Results and discussion

Figure 4 shows the temperature plots on the location of the three probes that were inserted inside the phantom. A model uncertainty of $\sigma_w^2 = 2$ is used for the POD-Kalman temperatures (dashed black lines), as this was found to produce the best results. The verification probes (yellow lines) indicate the actual temperature at the probe locations.

An immediate observation is that the assumption of zero-mean noise is not satisfied for the MRT (square markers). It shows a consistent deviation that varies with temperature and probe location. In probe 2 the filtered temperature shows an improvement over both MRT and simulated temperatures (round markers). Especially after water circulation (indicated by the last vertical line) the filtered temperature is not sensitive to the MRT noise. In probe 1 an improvement can be seen after the second heating focus is applied. Initially, however, the POD-Kalman temperature underestimates the heating rate, following both the POD-reduced simulation and the MRT. Interestingly, the POD-Kalman temperature does not lie between the MRT and simulated temperature. This can be explained by the modal coupling between all nodes that follows from the POD basis approach. The POD mode coefficients obtained after the measurement update can be interpreted as an "interpolation" of the modes through all points in the MRT slice. In probe 3, both MRT and simulation show significant error with respect to the verification temperatures, which is inherently reflected in the POD-Kalman temperature.

The resulting mean absolute error (MAE) and maximum errors for all probes are summarized in Table IV. The filtered results (PKf) are shown for different values of model uncertainty σ_w^2. The impact of this weighting is found to be small. The reason for this is that both MRT and simulation accuracy vary with region and time. This can be seen in, for example, probe 2. The MRT shows an initial cooling when the first focus is applied. This implies a negative PRFS shift, which is erroneous. After the second focus has been applied, the simulation slope does not match that of the verification probe, whereas the MRT becomes more accurate. A difference in slope between verification and simulation suggests a model mismatch. This mismatch is likely to be caused by a combination of input (SAR) uncertainty and model parameter uncertainty. The result of this uncertainty will also be reflected in the POD modes, which restricts the degrees-of-freedom that MRT can incorporate in the correction step. Maximum temperature errors range from 12.7 °C for the MRT (when water circulation is on) to 2.43 °C for the filtered temperature ($\sigma_w^2 = 2$), which is slightly lower than for the forward simulation (2.74 °C). The filtered temperature also shows an improvement in MAE, going from 1.65 °C (MRT) and 1.41 °C (simulation) to 1.03 °C.

In Fig. 5, the norm of the innovation gain is shown. It indicates that the spatial estimation of the measurement error results in very low gains when the water is circulated. This is illustrated by the temperature plots in Figure 4, where the POD-Kalman update disregards most of the MRT images and relies on simulation instead. This strategy results in some improvement for the POD-Kalman estimate after water circulation is turned on. Better simulation or MRT data in probe location 3 would likely have resulted in better filter estimates. A plausible explanation for the temperature error in these regions for the MRT is that the temperature in that region varies strongly with position (large gradient). Furthermore, we experienced some difficulty in locating probes that are located further from the center of the image. This is caused by a slight spatial warping (barrel distortion) of the MR images that may be corrected in future work using image processing techniques. Furthermore, an important question is whether improvements in the choice of POD basis simulations could yield better results. While an improved POD basis with a more structural excitation (i.e., more different

TABLE IV

MEAN ABSOLUTE AND (MAXIMUM) ERRORS OF THE RAW MRT, THE FORWARD SIMULATED POD-REDUCED MODEL (SIM) AND THE POD-KALMAN FILTERED (PKF) TEMPERATURES. THE ERRORS ARE CALCULATED FOR THE THREE COMBINED PROBES OVER ALL TIME POINTS, AND THE INTERVALS WITHOUT WATER CIRCULATION AND WITH WATER CIRCULATION ARE SHOWN BOTH SEPARATELY AND COMBINED.

	MRT	Sim.	PKf, $\sigma_w^2 = 0.5$	PKf, $\sigma_w^2 = 2$	PKf, $\sigma_w^2 = 5$
Water circ. off	1.27	1.24	1.05	0.99	0.99
	(2.56)	(2.72)	(2.38)	(2.31)	(2.31)
Water circ. on	2.60	1.97	1.10	1.14	1.18
	(12.7)	(2.73)	(2.46)	(2.42)	(2.44)
Total	1.65	1.42	1.06	1.03	1.03
	(12.7)	(2.73)	(2.46)	(2.42)	(2.44)

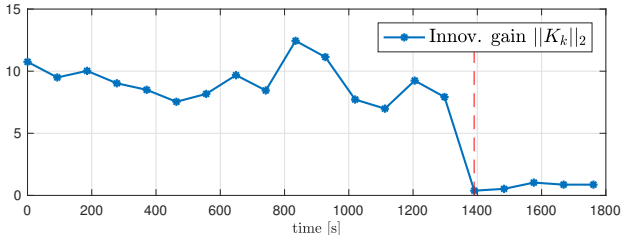

Fig. 5. The norm of the innovation gain K_k for the MRT updates, quantifying how much is relied on the MRT data in the new temperature estimate at time t_k.

input settings or model parameters) might show better results, it is not expected to yield a major improvement, since the error in the probe locations is mostly related to MRT readings and simulation updates. The recursive POD-Kalman strategy relies on MRT and simulation for estimates and if both are not physically accurate the strategy will not yield satisfactory results, regardless of the modal representation. The model update uncertainty is explicitly needed in the Kalman update equations and the assumption of a diagonal covariance matrix in this work is only a rough estimate. Improvements in this area may be possible by explicitly incorporating parameter uncertainty of the EM model and the thermal model to estimate temperature uncertainties for specific regions. Whether these uncertainties can be well reflected in the modal structure of the POD model is to be investigated.

VI. CONCLUSIONS AND FUTURE WORK

In this paper, POD-Kalman filtering of MRT data is proposed for RF hyperthermia and is found to reduce the mean absolute temperature error in a phantom experiment by 38%. It can be stated that the approach of POD-Kalman filtering of the temperature response can provide potential benefits over the use of only MR thermometry. The preliminary results show the potential of the proposed techniques and inspire us to carry out future work. In particular, more research is needed into the mismatch between simulation and experiment and the image distortion near the edges should be dealt with. Furthermore, while a model reduction step is necessary to prevent the Kalman equations from becoming computationally prohibitive, it inherently limits the temperature distributions that are supported due to the reduced basis approach. This may pose the an important challenge when translating these experimental results to actual patient treatments. While acquiring accurate and verified models of the temperature reponse in patients is a subject outside of the scope of this work, it is stressed that the availability of these models is a prerequisite for the proposed technique to be applicable in clinical procedures. Moreover, more advanced post processing of the MRT may yield the most significant improvement on short notice, and should also be seen as a prerequisite for the recursive estimation strategy to produce acceptable results and for possible future adaptation to clinical use. Despite these remaining challenges the presented ideas and results are an important step towards enabling the use of POD-Kalman filtering and advanced control for hyperthermia in clinical use.

REFERENCES

[1] J. van der Zee, "Heating the patient: a promising approach?" *Annals of Oncology*, vol. 13, no. 8, pp. 1173–1184, 2002.

[2] J. van der Zee and G. C. van Rhoon, "Cervical cancer: Radiotherapy and hyperthermia," *Int. Journal of Hyperthermia*, vol. 22, no. 3, pp. 229–234, 2006.

[3] National Cancer Institute (2011). [Online]. Available: https://www.cancer.gov/about-cancer/treatment/types/surgery/hyperthermia-fact-sheet

[4] M. M. Paulides, P. R. Stauffer, E. Neufeld, P. F. Maccarini, A. Kyriakou, R. A. M. Canters, C. J. Diederich, J. F. Bakker, and G. C. van Rhoon, "Simulation techniques in hyperthermia treatment planning." *Int. Journal of Hyperthermia*, vol. 29, no. 4, pp. 346–57, 2013.

[5] K. S. Cheng, V. Stakhursky, P. Stauffer, M. Dewhirst, and S. K. Das, "Online feedback focusing algorithm for hyperthermia cancer treatment," *Int. Journal of Hyperthermia*, vol. 23, no. 7, pp. 539–554, 2007.

[6] K. S. Cheng, Y. Yuan, Z. Li, P. R. Stauffer, P. Maccarini, W. T. Joines, M. W. Dewhirst, and S. K. Das, "The performance of a reduced-order adaptive controller when used in multi-antenna hyperthermia treatments with nonlinear temperature-dependent perfusion," *Physics in Medicine and Biology*, vol. 54, no. 7, p. 1979, 2009.

[7] J. Gellermann, W. Wlodarczyk, H. Ganter, J. Nadobny, H. Fähling, M. Seebass, R. Felix, and P. Wust, "A practical approach to thermography in a hyperthermia/magnetic resonance hybrid system: Validation in a heterogeneous phantom," *Int. Journal of Radiation Oncology Biology Physics*, vol. 61, no. 1, pp. 267–277, 2005.

[8] J. Gellermann, W. Wlodarczyk, B. Hildebrandt, H. Ganter, A. Nicolau, B. Rau, W. Tilly, H. Fa, J. Nadobny, R. Felix, and P. Wust, "Noninvasive Magnetic Resonance Thermography of Recurrent Rectal Carcinoma in a 1 . 5 Tesla Hybrid System," *Cancer Research*, vol. 65, no. 13, pp. 5872–5880, 2005.

[9] V. Rieke and K. Butts Pauly, "MR Thermometry," *Journal for Magnetic Resonance Imaging*, vol. 27, no. 2, pp. 376–390, 2008.

[10] B. D. de Senneville, S. Roujol, C. Moonen, and M. Ries, "Motion correction in mr thermometry of abdominal organs: A comparison of the referenceless vs. the multibaseline approach," *Magnetic Resonance in Medicine*, vol. 64, no. 5, pp. 1373–1381, 2010.

[11] C. Bing, R. M. Staruch, M. Tillander, M. O. Köhler, C. Mougenot, M. Ylihautala, T. W. Laetsch, and R. Chopra, "Drift correction for accurate prf-shift mr thermometry during mild hyperthermia treatments with mr-hifu," *Int. Journal of Hyperthermia*, vol. 32, no. 6, pp. 673–687, 2016.

[12] J. K. Potocki and H. S. Tharp, "Application of extended kalman filtering to hyperthermia," in *Proc. of the 31st IEEE Conf. on Decision and Control*, 1992, pp. 1390–1391 vol.2.

[13] R. van Rooijen, "Parameter estimation for hyperthermia treatment planning using model-based observer design ," *MSc thesis, Eindhoven University of Technology*, 2016.

[14] S. Roujol, B. D. de Senneville, S. Hey, C. Moonen, and M. Ries, "Robust adaptive extended kalman filtering for real time mr-thermometry guided hifu interventions," *IEEE Trans. on Medical Imaging*, vol. 31, no. 3, pp. 533–542, March 2012.

[15] Y. Zhang, S. Chen, K. Deng, B. Chen, X. Wei, J. Yang, S. Wang, and K. Ying, "Kalman filtered bio heat transfer model based self-adaptive hybrid magnetic resonance thermometry," *IEEE Trans. on Medical Imaging*, vol. 36, no. 1, pp. 194–202, Jan 2017.

[16] W. A. Grissom, V. Rieke, A. B. Holbrook, Y. Medan, M. Lustig, J. Santos, M. V. McConnell, and K. B. Pauly, "Hybrid referenceless and multibaseline subtraction mr thermometry for monitoring thermal therapies in moving organs," *Medical Physics*, vol. 37, no. 9, pp. 5014–5026, 2010.

[17] A. Antoulas, *Approximation of Large-Scale Dynamical Systems*. Society for Industrial and Applied Mathematics, 2005.

[18] R. Niu and M. Skliar, "Image-based identification of low-dimensional pod models of noninvasive thermal therapies," in *2006 American Control Conference*, 2006.

[19] P. M. A. van Haaren, H. P. Kok, C. A. T. van den Berg, P. J. Zum Vörde Sive Vörding, S. Oldenborg, L. J. A. Stalpers, M. S. Schilthuis, A. A. C. de Leeuw, and J. Crezee, "On verification of hyperthermia treatment planning for cervical carcinoma patients," *Int. Journal of Hyperthermia*, vol. 23, no. 3, pp. 303–314, 2007.

[20] J. Gellermann, P. Wust, D. Stalling, M. Seebass, J. Nadobny, R. Beck, H.-C. Hege, P. Deuflhard, and R. Felix, "Clinical evaluation and verification of the hyperthermia treatment planning system hyperplan," *Int. Journal of Radiation Oncology and Biological Physics*, vol. 47, no. 4, pp. 1145 – 1156, 2000.

[21] R. A. M. Canters, M. M. Paulides, M. Franckena, J. W. Mens, and G. C. van Rhoon, "Benefit of replacing the sigma-60 by the sigma-eye applicator," *Strahlentherapie und Onkologie*, vol. 189, no. 1, pp. 74–80, Jan 2013.

[22] H. H. Pennes, "Analysis of tissue and arterial blood temperatures in the resting human forearm," *Journal of Applied Physiology*, vol. 1, no. 2, pp. 93–122, 1948.

[23] M. S. Grewal and A. P. Andrews, *Kalman Filtering: Theory and Practice with MATLAB*, 4th ed. Wiley-IEEE Press, 2014.